# Propagatable Hierarchical Architectures from Dispersive Fragments to Periodic Nanosheets within Phase-Separated Nanostructures by Controlling Guest−Host Interaction

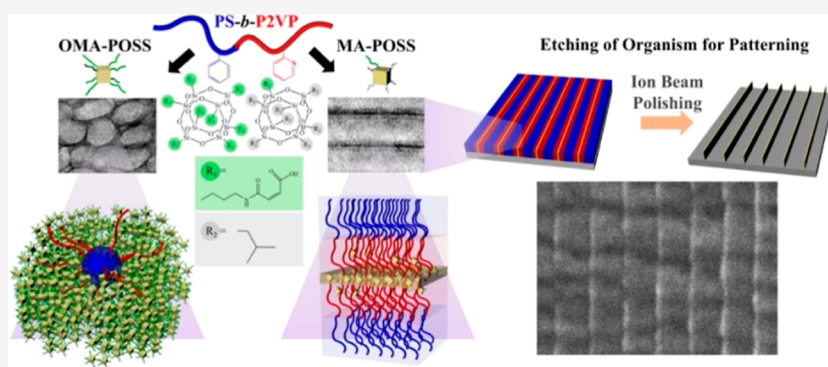I-Ming Lin, Chih-Chiang Hsu, Tsung-Chun Yu, Shiao-Wei Kuo, Wei-Tsung Chuang, and Yeo-Wan Chiang*

Read Online

ACCESS | Metrics & More | Article Recommendations | Supporting Information

**ABSTRACT:** Nanomaterials with a hierarchical organization of multiple scales are critical for reducing line width in semiconductor manufacturing. We design nanohybrid materials with a hierarchical or homogeneous phase of polyhedral oligomeric silsesquioxane (POSS) nanoparticles by controlling guest−host and guest−guest interactions. The guest POSS nanoparticle with the single-acid-terminated (MA−POSS) or octa-acid-terminated (OMA−POSS) functionality is introduced into a host polystyrene-*block*-poly(2-vinylpyridine) (PS-*b*-P2VP) block copolymer. As the MA−POSS concentration is low, the stronger self-association (guest−guest interaction) between the MA−POSS nanoparticles and the weaker hydrogen bonding force (guest−host interaction) between the P2VP and the MA−POSS result in the formation of dispersive fragments in the chain end of the P2VP block. With increasing MA−POSS concentration, the fragment can grow into a single nanosheet parallel to the lamellar P2VP microdomain and then continuously develop into the periodic tri-nanosheet and quadro-nanosheet. In contrast, introducing the octa-acid-terminated OMA−POSS with enhanced guest−host interaction leads to the homogeneous dispersion of the OMA−POSS cluster in the P2VP microdomain, independent of the OMA−POSS concentration. Moreover, owing to distinct etch contrast among the inorganic POSS and the organic block copolymer, the well-defined line pattern of nanosheets of a few nanometers can be observed. Consequently, the hierarchical structures with the propagatable nanosheet of ∼4 nm or homogeneous dispersion of the POSS nanoparticles within the microphase-separated P2VP microdomain can be well controlled, providing a means of designing nanohybrid materials with distinct distributions of the functional nanoparticles.
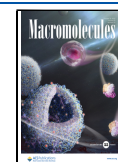
## 1. INTRODUCTION

Block copolymers (BCPs) possessing the chemical linkage to polymers of different chemical and physical properties could exhibit various self-assembled microstructures such as lamellar, gyroid, hexagonally packed cylinder, and spherical phases, dependent on Flory−Huggins interaction parameter ($\chi$), the degree of polymerization ($N$), and the composition or volume fraction ($f$).[1,2] To elevate the performance of thermal, optoelectronic, and magnetic properties,[3−5] BCP-based supramolecules with tunable inherent properties by incorporation with additives provide a feasible approach instead of the effort of synthesis. BCP-based supramolecules are formed through secondary interactions among organic or inorganic guests of specific functionalities and a host block chain of BCPs, revealing unique chemical and physical properties for different applications. The competition between the attractive and repulsive forces between the host polymer and the guest is critical for affecting the dispersion of guests such as homogeneous, localized, or structure-within-structure in the
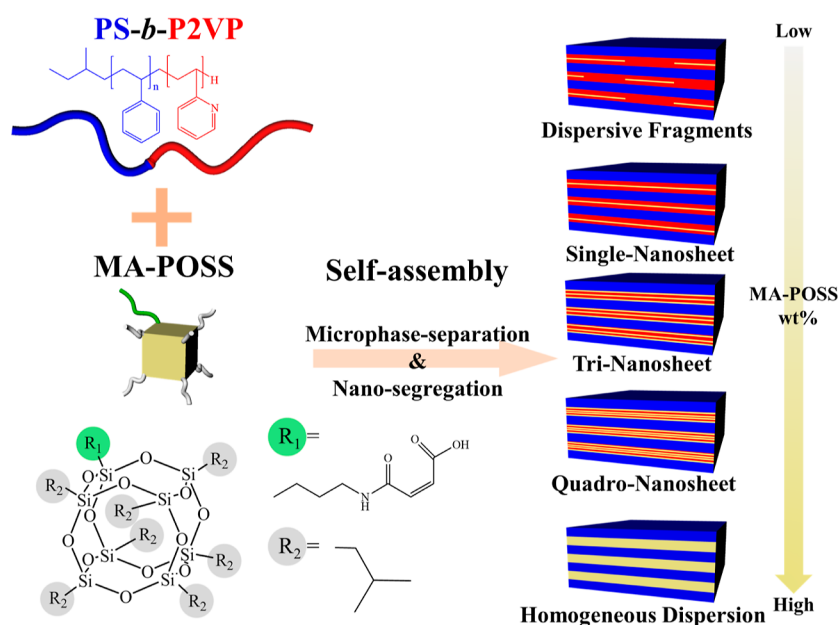
**Figure 1.** Schematic hierarchical architectures of PS-*b*-P2VP(MA−POSS) nanohybrids with propagating fragments and nanosheets within microphase-separated lamella with the increase in the composition of the MA−POSS nanoparticle.
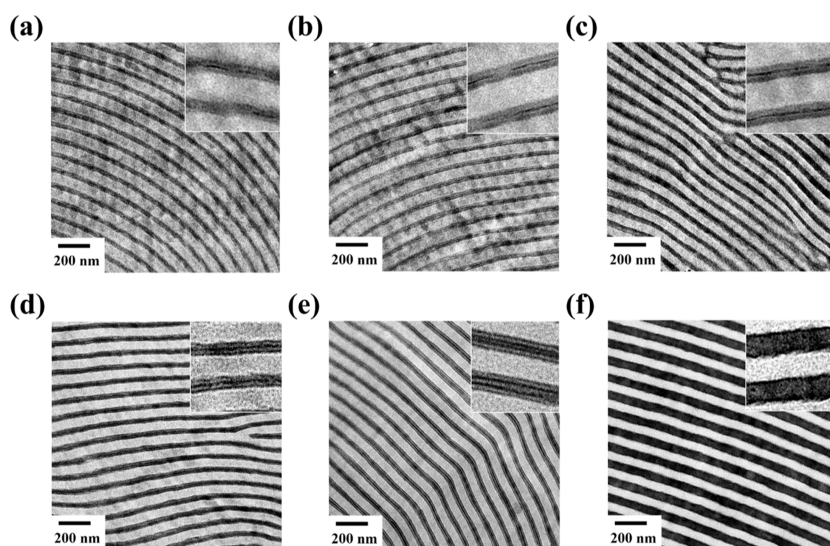


**Figure 2.** TEM micrographs of the PS-*b*-P2VP(MA−POSS) nanohybrids with various weight fractions of MA−POSS cast from chloroform. (a) 3 wt % ($f_{PS}^{v}$ = 0.57), (b) 7 wt % ($f_{PS}^{v}$ = 0.54), (c) 10 wt % ($f_{PS}^{v}$ = 0.53), (d) 15 wt % ($f_{PS}^{v}$ = 0.50), (e) 20 wt % ($f_{PS}^{v}$ = 0.47), and (f) 30 wt % ($f_{PS}^{v}$ = 0.41). After I$_2$ staining, P2VP(MA−POSS) microdomains are dark and PS microdomains are bright.

self-assembled morphologies.[6−10] For instance, organic surfactants or mesogens could strongly associate polar polymer block chains through ionic or hydrogen bonding forces to form organic nanohybrids, exhibiting light-responsive, conductive, or sensing properties.[11−15] To further extend the optoelectronic, catalytical, or sensing properties, inorganic guests are introduced into BCPs to form organic/inorganic nanohybrids.[16−19] However, the precise location and the packing geometry of the inorganic additives in the preferential microdomain are hard to be controlled due to the complicated competition between homogeneous and heterogeneous intermolecular interactions, influencing the final performance of the nanohybrid.[20−23]

Inorganic polyhedral oligomeric silsesquioxanes (POSSs) possess a unique cage-like structure of 1−3 nm nanoscale and

are promising in elevating the thermal and mechanical properties of polymers and reducing the line width for nanopatterning. With the designed organic substituents on the outer surface of POSS, the functionalized POSS can be selectively compatible with various polymers to form organic/inorganic nanohybrid materials, and it reveals the distinct properties of etching contrast, catalysis, and photonic crystal.[24−30] Previous studies mainly investigated the octa-functionalized phenol POSS (OP−POSS) nanoparticles on the phase behavior of the hybrid self-assemblies of various diblock copolymers, such as poly(styrene-*block*-4-vinylpyridine) (PS-*b*-P4VP), poly(styrene-*block*-2-vinylpyridine) (PS-*b*-P2VP), and poly(styrene-*block*-methylmethacrylate) (PS-*b*-PMMA). These systems indicated the homogeneous dispersion of the OP-
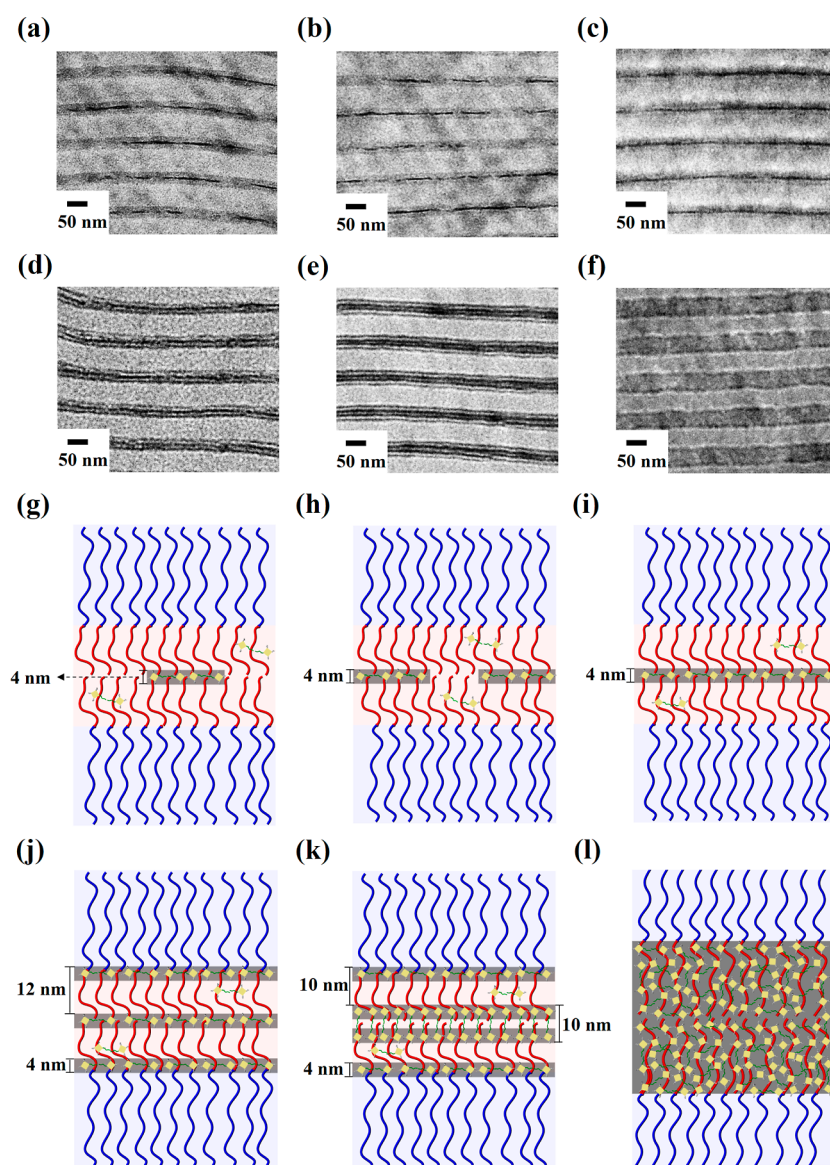
**Figure 3.** TEM micrographs of the unstained PS-*b*-P2VP(MA−POSS) nanohybrids with various weight fractions of MA−POSS cast from chloroform. (a) 3 wt % ($f_{PS}^v$ = 0.57), (b) 7 wt % ($f_{PS}^v$ = 0.54), (c) 10 wt % ($f_{PS}^v$ = 0.53), (d) 15 wt % ($f_{PS}^v$ = 0.50), (e) 20 wt % ($f_{PS}^v$ = 0.47), and (f) 30 wt % ($f_{PS}^v$ = 0.41). Without staining, the MA−POSS nanoparticles are dark and the PS and the P2VP are bright. The corresponding propagating schematic of MA−POSS nanoparticles in the P2VP microdomain. (g) Loosely dispersed short fragment, (h) densely dispersed long fragment, (i) single nanosheet, (j) tri-nanosheet, (k) quadro-nanosheet, and (l) homogeneous dispersion. The blue chain, red chain, and yellow cube represent the PS block chain, the P2VP block chain, and the MA−POSS nanoparticle, respectively.

POSS within the preferential P4VP, P2VP, and PMMA microdomains due to hydrogen bonding interaction.[31−33]

Here, we systematically investigated BCP-based supra-molecules consisting of acid-terminated POSS and PS-*b*-P2VP. The PS-*b*-P2VP BCP associated with the POSS molecules having different numbers of terminated acids, including maleamic acid−isobutyl POSS (MA−POSS) and octa-maleamic acid POSS (OMA−POSS), could result in distinct final nanostructures due to the consequence of guest−guest or guest−host hydrogen bonding interaction. The novel hierarchical architecture with propagating fragments and nanosheets was first developed by the self-alignment and aggregation of the POSS nanoparticles. The followed homogeneous dispersion was obtained, strongly dependent on the composition of the POSS additive.

## 2. RESULTS AND DISCUSSION

The microphase-separated structures of the PS-*b*-P2VP bulk sample cast from chloroform were investigated by small-angle X-ray scattering (SAXS) and transmission electron microscopy (TEM). In Figure S1a, the TEM micrograph of the as-cast PS-*b*-P2VP revealed the long-range-order gyroid microstructure along the [110] direction. After I$_2$ staining, the P2VP microdomains appear dark and the PS microdomains are bright. The corresponding SAXS profile (Figure S1b) also reveals the relative $q$ ratio of $\sqrt{6}:\sqrt{8}:\sqrt{14}$ of the double gyroid phase. Introducing an additive that is highly compatible with one of the blocks can effectively manipulate the self-assembled morphology. Here, the PS-*b*-P2VP BCP was first blended with the MA−POSS that is expected to be hydrogen-bonded with the P2VP block chains (Figure 1). By introducing 3 wt % MA−POSS into the PS-*b*-P2VP BCP, denoted as PS-*b*-

P2VP(MA−POSS)$_{3 \text{ wt \%}}$, a phase transition from the double gyroid to the lamellae is obtained (Figure 2a). After I$_2$ staining, the P2VP(MA−POSS) appears dark, and the PS is bright. Besides, this lamellar microstructure of the PS-b-P2VP(MA−POSS)$_{3 \text{ wt \%}}$ can be confirmed by the SAXS profile with a relative q ratio of 1:2:3:4 (Figure S2). Instead of homogeneous distribution as reported previously,[31−33] the MA−POSS guests could aggregate to form a hierarchical structure in the preferential P2VP microdomain. As shown in the inset of Figure 2a, the dispersive fragments of darker contrast can be clearly observed in the P2VP(MA−POSS) microdomain. The thickness of the fragment is 4 ± 0.5 nm, corresponding to the cage structure of the MA−POSS nanoparticle (∼4.6 nm). The unstained TEM images were further examined to investigate the origin of the fragments. In Figure 3a, the unstained TEM image of the PS-b-P2VP(MA−POSS)$_{3 \text{ wt \%}}$ also shows the dispersive fragment of dark contrast. In the unstained TEM image, the contrast is mainly dominated by the atomic number, indicating the dark MA−POSS due to the heavier Si atom and the bright PS-b-P2VP due to the light elements of the organism. As a result, the dark fragments are due to the aggregation of the additive MA−POSS nanoparticles in the P2VP(MA−POSS) microdomain.

With increasing the weight fraction of the MA−POSS to 7 wt %, the previous short dispersive fragments could form long dispersive fragments within the lamellar morphology of the PS-b-P2VP(MA−POSS)$_{7 \text{ wt \%}}$ (Figure 2b). By further increasing the quantity of MA−POSS to 10 wt %, we observed the unchanged lamellar structure in the PS-b-P2VP(MA−POSS)$_{10 \text{ wt \%}}$, consistent with the corresponding lamellar SAXS profiles in Figure S2. Interestingly, the long dispersive fragments could transfer into a continuous single nanosheet segregated in the center of the P2VP microdomain (Figure 2c). The insets in Figure 2a−c show the development from the short fragment to the long fragment and a single nanosheet by the self-alignment and aggregation of the MA−POSS nanoparticles located in the center region of the P2VP microdomain as the MA−POSS concentration is low (3−10 wt %). Also, the corresponding unstained TEM image of high magnification shows the consistent phase transition from the dispersive fragment to the single nanosheet, in Figure 3b,c. Except for the central fragment or nanosheet, we also found the gray contrast in the P2VP microdomain. This suggests that some MA−POSS nanoparticles may uniformly disperse in the P2VP block chains.

With continuously increasing the MA−POSS to 15 wt %, the lamellar microstructures can still be obtained in the PS-b-P2VP(MA−POSS)$_{15 \text{ wt \%}}$ (Figure 2d), as proved by the SAXS profile (Figure S2). Notably, instead of the single MA−POSS nanosheet, the tri-nanosheet of alternating parallel arrangement is obtained in the P2VP microdomain. Not only the central nanosheet but also the two extra nanosheets in the interfaces between the PS and P2VP(MA−POSS) microdomains appear in the inset of Figure 2d. As measured, the tri-nanosheet has a regular periodicity of 12 ± 1 nm. The MA−POSS nanosheets observed in the interfaces might sometimes be artificial due to the edge effect of staining. Therefore, the unstained TEM image was helpful for further confirmation. In Figure 3d, the unstained TEM image of the PS-b-P2VP(MA−POSS)$_{15 \text{ wt \%}}$ still shows the tri-nanosheet of the MA−POSS nanoparticles self-aligned in the center and interfaces of the P2VP microdomain. In comparison, the dispersive fragments or the nanosheets are absent in the interfaces between the PS

and P2VP block chains in the unstained TEM images as the MA−POSS concentration is low such as 3, 7, and 10 wt % in Figure 3a−c. As a result, the unstained TEM results verify the formation of this unique hierarchical tri-nanosheet within the P2VP microdomain. As the MA−POSS concentration further increased to 20%, the tri-nanosheet could further propagate into the quadro-nanosheet in the preserved lamella-structured PS-b-P2VP(MA−POSS)$_{20 \text{ wt \%}}$ (Figures 2e and 3e). Regarding the morphological stability, we performed the thermal annealing treatment at 150 °C for 12 h on PS-b-P2VP(MA−POSS)$_{20 \text{ wt \%}}$. In Figure S3, the same lamellar morphology is still obtained after thermal annealing, suggesting the equilibrium state. Unlike the regular periodicity in the tri-nanosheet, the quadro-nanosheet texture presents two distinct distances. As the weight fraction of the MA−POSS is 30 wt %, the lamellar morphology remained in the PS-b-P2VP(MA−POSS)$_{30 \text{ wt \%}}$ (Figure 2f). However, the inset in Figure 2f presents homogeneous dark contrast in the P2VP(MA−POSS) microdomains, consistent with the unstained TEM image in Figure 3f. This suggests that a large amount of MA−POSS nanoparticles are uniformly distributed in the P2VP microdomain (Figure 3l). As shown in Figure S4, low-magnification images with a 3*3 μm$^2$ area confirmed the long-range-order nanosheet-featured lamellar microstructures because of the strong segregation strength of the PS−b−P2VP BCP and the casting process with a slow evaporation rate of the solvent. When the weight fraction of the MA−POSS reaches 40 and 50 wt %, we observed the phase transition from the lamellar morphology to the cylinder and the homogeneous distribution of the MA−POSS particles in both PS-b-P2VP(MA−POSS)$_{40 \text{ wt \%}}$ and PS-b-P2VP(MA−POSS)$_{50 \text{ wt \%}}$ nanohybrids (Figure S5a,b).

We suggest that the segregation of the dispersive fragments in the central region of the P2VP lamellae is the competitive consequence between the attractive hydrogen bonding interaction by the maleamic substitute and repulsive incompatibility by the isobutyl substitute. Although the single acid-terminated maleamic substitute could strongly associate with the pyridine of the P2VP block chain, the seven isobutyl substitutes on the surface of the MA−POSS may generate strong incompatibility or self-aggregation to force the P2VP chains to release out the MA−POSS nanoparticles. The released MA−POSS nanoparticles are further localized in the chain end of the P2VP, accompanying weak hydrogen bonding due to steric hindrance of the ortho-position of the P2VP (Figure 3g−i). As the end chain of the P2VP block is fully loaded, the excessive MA−POSS nanoparticles may migrate to the interfaces between the PS and the P2VP microdomains, resulting in the appearance of the tri-nanosheet (Figure 3j). This is attributed to the intensified hydrophobic interaction between the PS and the MA−POSS as the quantity of the MA−POSS is high. Once the loading of the interface is saturated, the nanosheet in the central region may turn into dual nanosheets of large capacity by stacking of dimer structures among the MA−POSS nanoparticles to form the quadro-nanosheet in Figure 3k. As measured, the length between the second and the third nanosheets is 10 ± 1 nm, similar to the dimer structure of the MA−POSS nanoparticles (∼9.2 nm) (Figure 3k). However, as the MA−POSS nanoparticles are overloaded, homogeneous dispersion of the MA−POSS nanoparticles in the P2VP microdomain is observed (Figure 3l).
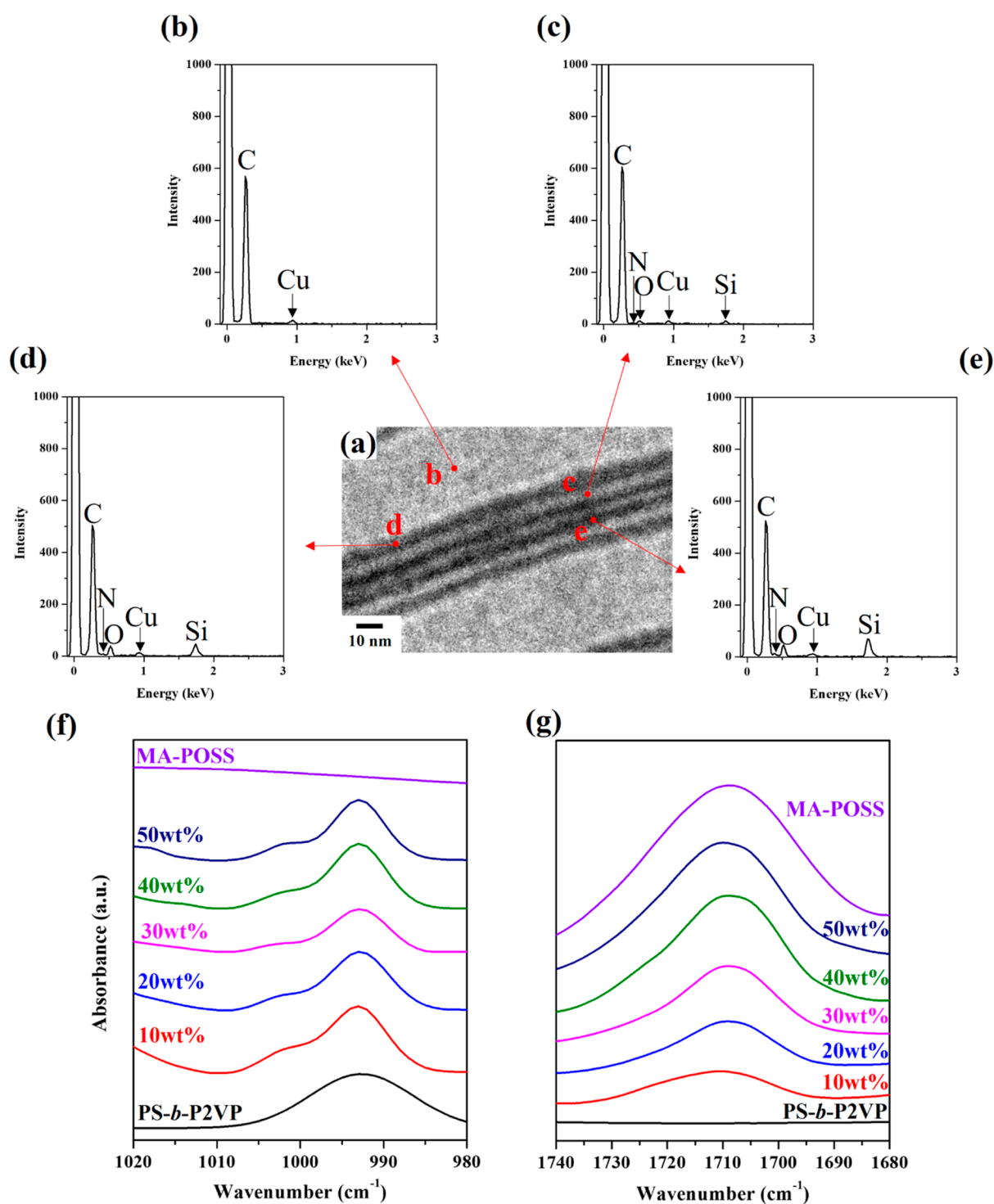
**Figure 4.** (a) Unstained TEM micrograph of the PS-*b*-P2VP(MA−POSS)$_{20 \text{ wt } \%}$ nanohybrid and the corresponding NBEDS profiles measured from different regions including the (b) bright PS microdomain, (c) gray P2VP microdomain, (d) first dark nanosheet in the interfacial region, and (e) third dark nanosheet. FTIR spectra of a series of PS-*b*-P2VP(MA−POSS) nanohybrids with various weight fractions of the MA−POSS nanoparticle. (f) 980 to 1020 cm$^{-1}$ and (g) 1680 to 1760 cm$^{-1}$.

To further confirm the distribution of the MA−POSS nanoparticles, we conducted nanobeam energy-dispersive X-ray spectroscopy (NBEDS) on the representative case of the quadro-nanosheet in the PS-*b*-P2VP(MA−POSS)$_{20 \text{ wt } \%}$ (Figure 4a). In Figure 4b, the NBEDS profile shows the strong signal of the C atom at 0.28 keV, while the nanobeam of the electron is precisely irradiated on the PS microdomain. No Si and O signals are acquired in the PS microdomain. While the nanobeam is focused on the gray region of the P2VP microdomain, the NBEDS profile exhibits the strong C signal due to the P2VP and the weak Si and O signals at 1.74 and 0.53 keV, respectively (Figure 4c). Similar to the gray contrast of the unstained TEM image, the weak Si and O signals again confirm that some MA−POSS nanoparticles are randomly distributed in the P2VP block chains. In contrast, while the nanobeam is focused on the first or the third dark nanosheet,

the strong C signal and the significant Si and O signals can be obtained (Figure 4d,e). As a result, the MA−POSS nanoparticles could selectively localize in the central and interfacial regions, depending on the additive quantity of the MA−POSS.

We investigated the hydrogen bonding interaction in the PS-b-P2VP(MA−POSS) system by Fourier transform infrared spectrometry (FTIR). In Figure 4f, the FTIR spectra ranging from 980 to 1020 cm$^{-1}$ show the most influential band for the stretching mode of the pyridine ring of the P2VP at 993 cm$^{-1}$. The neat PS-b-P2VP shows an absorption band at 993 cm$^{-1}$, representing the free pyridine unit. After introducing the MA−POSS of 10 wt %, a new absorption band at 1002 cm$^{-1}$ appears, representing the association between the P2VP unit and the MA−POSS nanoparticle by hydrogen bonding.[8] However, with the increase in the weight fraction of the MA−POSS, the intensity of the free pyridine stretching at 993 cm$^{-1}$ and hydrogen-bonded stretching at 1002 cm$^{-1}$ almost remains unchanged in all the PS-b-P2VP(MA−POSS) nanohybrids, indicating that the quantity of the MA−POSS associated with the P2VP is unchanged. In contrast, the high-wavenumber FTIR spectra ranging from 1680 to 1760 cm$^{-1}$ (Figure 4g) reveal the significant C=O stretching signal at around 1709 cm$^{-1}$ due to the vibration of the hydrogen-bonding interaction among the maleamic acid groups of the MA−POSS themselves, namely, the dimer structure.[7] As a result, the self-association (guest−guest interaction) between the MA−POSS is stronger than the hydrogen bonding force (guest−host interaction) between the P2VP and the MA−POSS in the PS-b-P2VP(MA−POSS) nanohybrids. This may lead to the dimer structure of the MA−POSS nanoparticles aggregating in the chain end of the P2VP block.

Taking advantage of the etching contrast between the PS-b-P2VP and POSS nanoparticles, the layer pattern with different width ratios can be carried out using nanosheets or homogeneous dispersion of the MA−POSS in the PS-b-P2VP(MA−POSS) nanohybrids. After etching by ion beam, the organic part of the PS-b-P2VP is removed and the inorganic part of the MA−POSS particles is preserved due to the distinct etching contrast (Figure 5a,b). In Figure 5c, the field emission scanning electron microscopy (FESEM) image of the etched PS-b-P2VP(MA−POSS)$_{10 wt \%}$ clearly shows vertically oriented MA−POSS nanosheets of 6 nm and channels of 70 nm in width. The thickness ratio between the nanosheets and channels is about 1:12, revealing a high-width ratio pattern. In contrast, the FESEM image reveals the thick MA−POSS layers of 66 nm and channels of 20 nm in the dispersive phase of the PS-b-P2VP(MA−POSS)$_{30 wt \%}$ after etching (Figure 5d).

To explore the effect of functional groups of the POSS nanoparticle on the hierarchical architecture, we employed the octa-acid-terminated POSS (OMA−POSS) with eight substituents of maleamic acids for comparison. Because of the eight substituents of maleamic acids in OMA−POSS, the hydrophilicity of the OMA−POSS is much stronger than that of the MA−POSS, giving rise to poor solubility in chloroform. We thus utilized dimethylformamide (DMF) to dissolve the OMA−POSS and the PS-b-P2VP. The TEM micrograph (Figure 6a) and the corresponding SAXS profile with the relative q ratios of 1:2 (Figure S6) indicate the formation of the long-range-order lamellar morphology in the as-cast PS-b-P2VP from DMF. With introducing 10 wt % of the OMA−POSS, the long-range-order lamellae become short-range-order lamellae in the PS-b-P2VP(OMA−POSS)$_{10 wt \%}$ (Figure 6b).
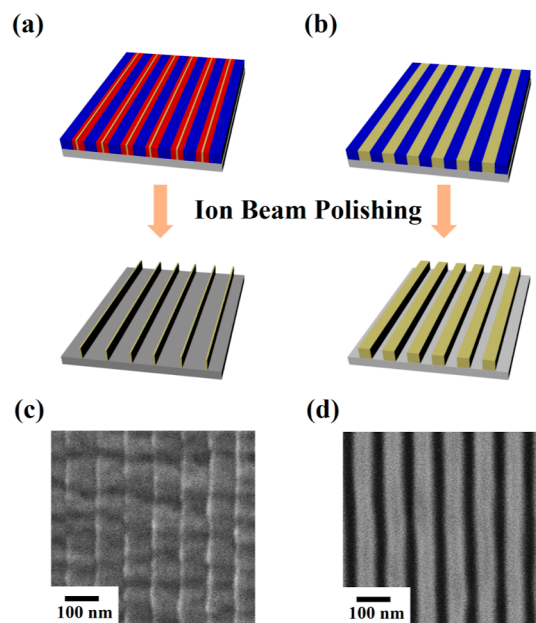


**Figure 5.** Schematic illustration for the fabrication of POSS nanosheets by etching of ion beam in (a) PS-b-P2VP(MA−POSS)$_{10 wt \%}$ and (b) PS-b-P2VP(MA−POSS)$_{30 wt \%}$. FESEM micrographs of (c) PS-b-P2VP(MA−POSS)$_{10 wt \%}$ and (d) PS-b-P2VP-(MA−POSS)$_{30 wt \%}$ after etching of ion beam.

The corresponding SAXS profile shows the lamellar reflection of a q ratio of 1:2 and the broad second peak (Figure S6). Besides, the TEM image presents the uniform dark contrast in the P2VP(OMA−POSS) microdomain, indicating the uniform dispersion of the additive OMA−POSS nanoparticles. When the weight fraction of the OMA−POSS reaches 20 wt %, we observed PS micelles embedding in the P2VP(OMA−POSS) matrix in the PS-b-P2VP(OMA−POSS)$_{20 wt \%}$ (Figure 6c). This is consistent with the broad reflective peaks (indicated by arrows) in the SAXS profile due to the scattering of the form factor (Figure S6). With further increasing the weight fraction of the OMA−POSS to 30, 40, and 50 wt %, similar PS micelles are obtained in the PS-b-P2VP(OMA−POSS)$_{30 wt \%}$, PS-b-P2VP(OMA−POSS)$_{40 wt \%}$, and PS-b-P2VP(OMA−POSS)$_{50 wt \%}$ (Figure 6d−f), respectively.

In Figure 6g, the FTIR spectrum of the PS-b-P2VP(OMA−POSS)$_{10 wt \%}$ shows that a new absorption band at 1003 cm$^{-1}$ is due to the association between the P2VP unit and the OMA−POSS in contrast to the free pyridine absorption of 993 cm$^{-1}$. With increasing the weight fraction of the OMA−POSS (20−50 wt %), the relative intensity of the free pyridine stretching at 993 cm$^{-1}$ decreased, and the relative intensity of the associated pyridine stretching at 1003 cm$^{-1}$ increased in the PS-b-P2VP(OMA−POSS) nanohybrids, being distinct from that in the PS-b-P2VP(MA−POSS) nanohybrid system. This expresses that the degree of the association between the OMA−POSS nanoparticle and P2VP chain gradually increases due to the large numbers of accessible bonding substitutes of the maleamic acids on the OMA−POSS nanoparticles. Moreover, the absorption band at around 1711 cm$^{-1}$ represents the hydrogen-bonded C=O stretching of the OMA−POSS cluster (Figure 6h). In contrast to the PS-b-P2VP(MA−POSS) nanohybrids, the guest−host interaction between the P2VP and the OMA−POSS intensifies with the increase in the additive OMA−POSS concentration in the PS-
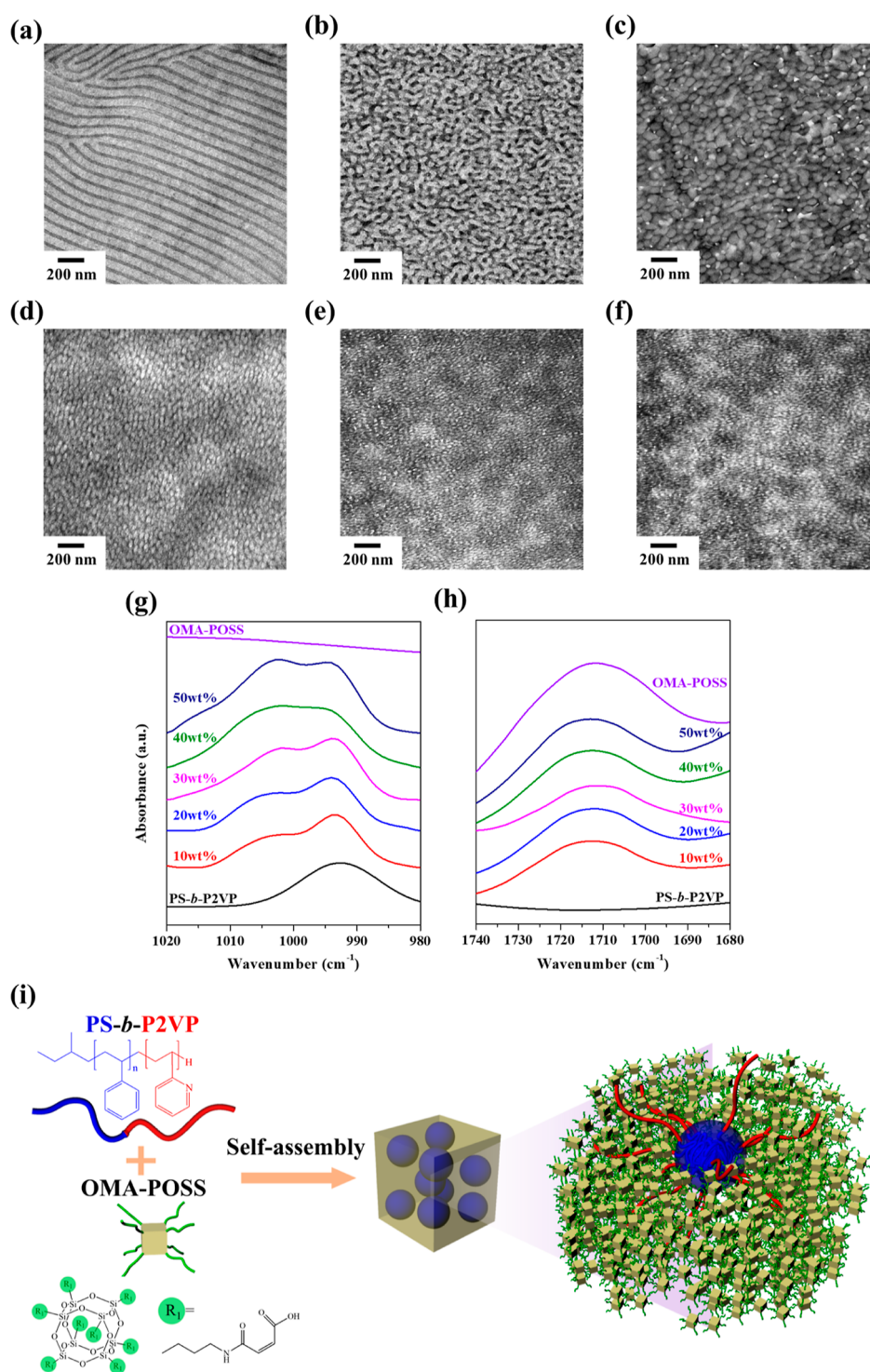
**Figure 6.** TEM micrographs of the PS-*b*-P2VP(OMA−POSS) nanohybrids with various weight fractions of OMA−POSS nanoparticles cast from DMF. (a) Neat PS-*b*-P2VP ($f_{PS}^v = 0.58$), (b) 10 wt % ($f_{PS}^v = 0.53$), (c) 20 wt % ($f_{PS}^v = 0.47$), (d) 30 wt % ($f_{PS}^v = 0.41$), (e) 40 wt % ($f_{PS}^v = 0.36$), and (f) 50 wt % ($f_{PS}^v = 0.30$). After I$_2$ staining, P2VP(OMA−POSS) is dark, and PS is bright. FTIR spectra of a series of the PS-*b*-P2VP(OMA−POSS) nanohybrids with various weight fractions of the OMA−POSS nanoparticle. (g) 980 to 1020 cm$^{-1}$ and (h) 1680 to 1760 cm$^{-1}$. (i) Schematic representation of the PS-*b*-P2VP(OMA−POSS) nanohybrids revealing the PS micelles embedded within the P2VP(OMA−POSS) matrix.

*b*-P2VP(OMA−POSS) nanohybrids. Therefore, this gives rise to a considerable enlargement in the effective volume fraction of the P2VP(OMA−POSS), and the PS micelles thus formed. However, a specified bonding site is absent for the OMA−POSS nanoparticle, resulting in the homogeneous distribution instead of forming hierarchical nanosheets (Figure 6i).

## 3. CONCLUSIONS

To the best of our knowledge, this is the first discovery that the POSS nanoparticles form the periodic nanosheets in the microphase-separated domain of BCPs. The number of hydrophilic and hydrophobic substitutes in the POSS nano-

particle is critical for manipulating the guest—guest and guest—host interactions, giving rise to a hierarchical architecture or homogeneous distribution in the nanohybrid materials. The MA—POSS nanoparticle of a single maleamic acid first aggregates into the dispersive fragments with an extendable length in the P2VP microdomain centrally as the MA—POSS concentration is low due to the specified binding site and stronger guest—guest interaction. As the MA—POSS concentration increases, the long dispersive fragments are connected to form the single nanosheet parallel to the lamellar interface. Further increasing the quantity of the MA—POSS induces the propagation into the tri- and quadro-nanosheet of periodic arrangement. As the MA—POSS concentration is above 30 wt %, the uniform dispersion of the MA—POSS is observed. In comparison, the OMA—POSS nanoparticle with octa-functionalized maleamic acids is always distributed uniformly in the P2VP microdomain due to the unspecified binding sites and stronger guest—host interaction. Owing to distinct etch contrast among the inorganic POSS and the organic BCP, the well-defined nanostructured pattern of nanosheets of a few nanometers can be observed. As a result, this concept of the propagatable periodic nanosheet of self-alignment could provide a means of designing nanohybrid materials with the precise distribution of the functional nanoparticle and reduce line width for lithographic and nanopatterning applications.

## ■ ASSOCIATED CONTENT

### Ⓢ Supporting Information

The Supporting Information is available free of charge at https://pubs.acs.org/doi/10.1021/acs.macromol.2c01643.

> Experimental details: materials, sample preparation, and characterization, TEM micrograph and SAXS profile of the neat PS-*b*-P2VP, SAXS profiles of the PS-*b*-P2VP(MA—POSS) and PS-*b*-P2VP(OMA—POSS) complexes, and TEM micrograph of the PS-*b*-P2VP-(MA—POSS)$_{40\ wt\ \%}$ and PS-*b*-P2VP(MA—POSS)$_{50\ wt\ \%}$ (PDF)

## ■ AUTHOR INFORMATION

### Corresponding Author

**Yeo-Wan Chiang** — *Department of Materials and Optoelectronic Science, National Sun Yat-Sen University, Kaohsiung 80424, Taiwan;* Ⓞ orcid.org/0000-0002-5409-102X; Email: ywchiang@mail.nsysu.edu.tw

### Authors

**I-Ming Lin** — *Department of Materials and Optoelectronic Science, National Sun Yat-Sen University, Kaohsiung 80424, Taiwan*

**Chih-Chiang Hsu** — *Department of Materials and Optoelectronic Science, National Sun Yat-Sen University, Kaohsiung 80424, Taiwan*

**Tsung-Chun Yu** — *Department of Materials and Optoelectronic Science, National Sun Yat-Sen University, Kaohsiung 80424, Taiwan*

**Shiao-Wei Kuo** — *Department of Materials and Optoelectronic Science, National Sun Yat-Sen University, Kaohsiung 80424, Taiwan;* Ⓞ orcid.org/0000-0002-4306-7171

**Wei-Tsung Chuang** — *National Synchrotron Radiation Research Center, Hsinchu 30076, Taiwan;* Ⓞ orcid.org/0000-0002-9000-2194

Complete contact information is available at:

https://pubs.acs.org/10.1021/acs.macromol.2c01643

### Notes

The authors declare no competing financial interest.

## ■ REFERENCES

(1) Bates, F. S.; Fredrickson, G. H. Block copolymers—designer soft materials. *Phys. Today* **1999**, *52*, 32−38.

(2) Park, C.; Yoon, J.; Thomas, E. L. Enabling nanotechnology with self assembled block copolymer patterns. *Polymer* **2003**, *44*, 6725−6760.

(3) Kuo, S.-W.; Wu, C.-H.; Chang, F.-C. Thermal properties, interactions, morphologies, and conductivity behavior in blends of poly(vinylpyridine)s and zinc perchlorate. *Macromolecules* **2004**, *37*, 192−200.

(4) Gu, P.-Y.; Jiang, Y.; Fink, Z.; Xie, G.; Hu, Q.; Kim, P. Y.; Xu, Q.-F.; Lu, J.-M.; Russell, T. P. Conductive thin films over large areas by supramolecular self-Assembly. *ACS Appl. Mater. Interfaces* **2020**, *12*, 54020−54025.

(5) Wakayama, H.; Yonekura, H.; Kawai, Y. Three-dimensional periodically ordered nanohetero metallic materials from self-assembled block copolymer composites. *ACS Macro Lett.* **2013**, *2*, 284−287.

(6) Ruokolainen, J.; Brinke, G. t.; Ikkala, O. Supramolecular polymeric materials with hierarchical structure-within-structure morphologies. *Adv. Mater.* **1999**, *11*, 777−780.

(7) Korhonen, J. T.; Verho, T.; Rannou, P.; Ikkala, O. Self-Assembly and hierarchies in pyridine-containing homopolymers and block copolymers with hydrogen-bonded cholesteric side-chains. *Macromolecules* **2010**, *43*, 1507−1514.

(8) Soininen, A. J.; Tanionou, I.; ten Brummelhuis, N.; Schlaad, H.; Hadjichristidis, N.; Ikkala, O.; Raula, J.; Mezzenga, R.; Ruokolainen, J. Hierarchical structures in lamellar hydrogen bonded LC side chain diblock copolymers. *Macromolecules* **2012**, *45*, 7091−7097.

(9) Chuang, W.-T.; Lo, T.-Y.; Huang, Y.-C.; Su, C.-J.; Jeng, U. S.; Sheu, H.-S.; Ho, R.-M. Directing the interfacial morphology of hierarchical structures of dendron-jacketed block copolymers via liquid crystalline phases. *Macromolecules* **2014**, *47*, 6047−6054.

(10) Lin, I. M.; Chou, C.-M.; Li, M.-C.; Guo, R.-H.; Lee, C.-K.; Li, H.-J.; Chiang, Y.-W.; Lin, Y.-H.; Lee, Y.-C.; Su, C.-J.; Jeng, U. S.; Chuang, W.-T. Superhelices with tunable twisting power directed from supramolecular pairing of focal asymmetry in achiral dendron-jacketed block copolymers. *J. Mater. Chem. C* **2020**, *8*, 1923−1932.

(11) Zhao, Y.; Thorkelsson, K.; Mastroianni, A. J.; Schilling, T.; Luther, J. M.; Rancatore, B. J.; Matsunaga, K.; Jinnai, H.; Wu, Y.; Poulsen, D.; Fréchet, J. M. J.; Paul Alivisatos, A.; Xu, T. Small-molecule-directed nanoparticle assembly towards stimuli-responsive nanocomposites. *Nat. Mater.* **2009**, *8*, 979−985.

(12) Arges, C. G.; Kambe, Y.; Suh, H. S.; Ocola, L. E.; Nealey, P. F. Perpendicularly aligned, anion conducting nanochannels in block copolymer electrolyte films. *Chem. Mater.* **2016**, *28*, 1377−1389.

(13) Kang, H. S.; Han, S. W.; Park, C.; Lee, S. W.; Eoh, H.; Baek, J.; Shin, D.-G.; Park, T. H.; Huh, J.; Lee, H.; Kim, D.-E.; Ryu, D. Y.; Thomas, E. L.; Koh, W.-G.; Park, C. 3D touchless multiorder

reflection structural color sensing display. *Sci. Adv.* **2020**, *6*, No. eabb5769.

(14) Lin, E.-L.; Hsu, W.-L.; Chiang, Y.-W. Trapping structural coloration by a bioinspired gyroid microstructure in solid state. *ACS Nano* **2018**, *12*, 485−493.

(15) Wu, C. S.; Tsai, P. Y.; Wang, T. Y.; Lin, E. L.; Huang, Y. C.; Chiang, Y. W. Flexible or robust amorphous photonic crystals from network-forming block copolymers for sensing solvent vapors. *Anal. Chem.* **2018**, *90*, 4847−4855.

(16) Bockstaller, M. R.; Mickiewicz, R. A.; Thomas, E. L. Block copolymer nanocomposites: perspectives for tailored functional materials. *Adv. Mater.* **2005**, *17*, 1331−1349.

(17) Zhang, L.; Cui, T.; Cao, X.; Zhao, C.; Chen, Q.; Wu, L.; Li, H. Inorganic-macroion-induced formation of bicontinuous block copolymer nanocomposites with enhanced conductivity and modulus. *Angew. Chem., Int. Ed.* **2017**, *56*, 9013−9017.

(18) Tseng, W.-H.; Chen, C.-K.; Chiang, Y.-W.; Ho, R.-M.; Akasaka, S.; Hasegawa, H. Helical nanocomposites from chiral block copolymer templates. *J. Am. Chem. Soc.* **2009**, *131*, 1356−1357.

(19) Liedel, C.; Pester, C. W.; Ruppel, M.; Lewin, C.; Pavan, M. J.; Urban, V. S.; Shenhar, R.; Bösecke, P.; Böker, A. Block copolymer nanocomposites in electric fields: kinetics of alignment. *ACS Macro Lett.* **2013**, *2*, 53−58.

(20) Kao, J.; Xu, T. Nanoparticle assemblies in supramolecular nanocomposite thin films: concentration dependence. *J. Am. Chem. Soc.* **2015**, *137*, 6356−6365.

(21) Kao, J.; Bai, P.; Chuang, V. P.; Jiang, Z.; Ercius, P.; Xu, T. Nanoparticle assemblies in thin films of supramolecular nanocomposites. *Nano Lett.* **2012**, *12*, 2610−2618.

(22) Jang, S. G.; Kramer, E. J.; Hawker, C. J. Controlled supramolecular assembly of micelle-like gold nanoparticles in PS-b-P2VP diblock copolymers via hydrogen bonding. *J. Am. Chem. Soc.* **2011**, *133*, 16986−16996.

(23) Kim, B. J.; Bang, J.; Hawker, C. J.; Chiu, J. J.; Pine, D. J.; Jang, S. G.; Yang, S.-M.; Kramer, E. J. Creating surfactant nanoparticles for block copolymer composites through surface chemistry. *Langmuir* **2007**, *23*, 12693−12703.

(24) Kuo, S.-W.; Chang, F.-C. POSS related polymer nanocomposites. *Prog. Polym. Sci.* **2011**, *36*, 1649−1696.

(25) Hirai, T.; Leolukman, M.; Liu, C. C.; Han, E.; Kim, Y. J.; Ishida, Y.; Hayakawa, T.; Kakimoto, M.-a.; Nealey, P. F.; Gopalan, P. One-step direct-patterning template utilizing self-assembly of POSS-containing block copolymers. *Adv. Mater.* **2009**, *21*, 4334−4338.

(26) Tegou, E.; Bellas, V.; Gogolides, E.; Argitis, P.; Eon, D.; Cartry, G.; Cardinaud, C. Polyhedral oligomeric silsesquioxane (POSS) based resists: material design challenges and lithographic evaluation at 157 nm. *Chem. Mater.* **2004**, *16*, 2567−2577.

(27) Chae, C.-G.; Yu, Y.-G.; Seo, H.-B.; Kim, M.-J.; Grubbs, R. H.; Lee, J.-S. Experimental formulation of photonic crystal properties for hierarchically self-assembled POSS−bottlebrush block copolymers. *Macromolecules* **2018**, *51*, 3458−3466.

(28) Song, D.-P.; Naik, A.; Li, S.; Ribbe, A.; Watkins, J. J. Rapid, Large-area synthesis of hierarchical nanoporous silica hybrid films on flexible substrates. *J. Am. Chem. Soc.* **2016**, *138*, 13473−13476.

(29) Hirai, T.; Leolukman, M.; Jin, S.; Goseki, R.; Ishida, Y.; Kakimoto, M.-a.; Hayakawa, T.; Ree, M.; Gopalan, P. Hierarchical self-assembled structures from POSS-containing block copolymers synthesized by living anionic polymerization. *Macromolecules* **2009**, *42*, 8835−8843.

(30) Ahn, B.; Hirai, T.; Jin, S.; Rho, Y.; Kim, K.-W.; Kakimoto, M.-a.; Gopalan, P.; Hayakawa, T.; Ree, M. Hierarchical Structure in Nanoscale Thin films of a poly(styrene-b- methacrylate grafted with POSS) (PS$_{214}$-b-PMAPOSS$_{27}$). *Macromolecules* **2010**, *43*, 10568−10581.

(31) Lu, Y.-S.; Yu, C.-Y.; Lin, Y.-C.; Kuo, S.-W. Hydrogen bonding strength of diblock copolymers affects the self-assembled structures with octa-functionalized phenol POSS nanoparticles. *Soft Matter* **2016**, *12*, 2288−2300.

(32) Lu, Y.-S.; Kuo, S.-W. Functional groups on POSS nanoparticles influence the self-assembled structures of diblock copolymer composites. *RSC Adv.* **2014**, *4*, 34849−34859.

(33) Yu, C.-Y.; Kuo, S.-W. Phenolic functionality of polyhedral oligomeric silsesquioxane nanoparticles affects self-assembly supramolecular structures of block copolymer hybrid complexes. *Ind. Eng. Chem. Res.* **2018**, *57*, 2546−2559.

## ⬚ Recommended by ACS